

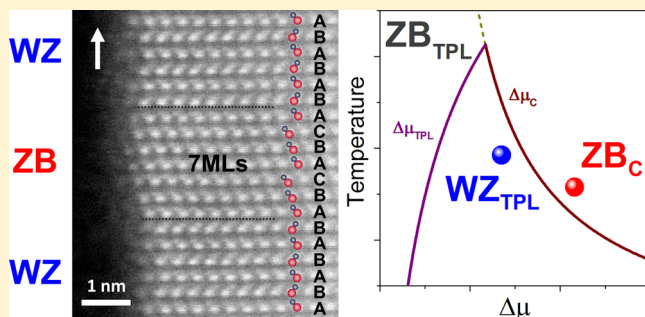
## Exploring Crystal Phase Switching in GaP Nanowires

S. Assali,<sup>\*,†</sup> L. Gagliano,<sup>†</sup> D. S. Oliveira,<sup>‡</sup> M. A. Verheijen,<sup>†,§</sup> S. R. Plissard,<sup>||</sup> L. F. Feiner,<sup>†</sup> and E. P. A. M. Bakkers<sup>†,⊥</sup><sup>†</sup>Department of Applied Physics Eindhoven, University of Technology, 5600 MB Eindhoven, The Netherlands<sup>‡</sup>Instituto de Física “Gleb Wataghin”, Universidade Estadual de Campinas, UNICAMP, 13083-859 Campinas, São Paulo, Brazil<sup>§</sup>Philips Innovation Services Eindhoven, High Tech Campus 11, 5656AE Eindhoven, The Netherlands<sup>||</sup>CNRS-Laboratoire d'Analyse et d'Architecture des Systèmes (LAAS), Université de Toulouse, 7 avenue du colonel Roche, F-31400 Toulouse, France<sup>⊥</sup>Kavli Institute of Nanoscience, Delft University of Technology, 2600 GA Delft, The Netherlands

## Supporting Information

**ABSTRACT:** The growth of wurtzite/zincblende (WZ and ZB, respectively) superstructures opens new avenues for band structure engineering and holds the promise of digitally controlling the energy spectrum of quantum confined systems. Here, we study growth kinetics of pure and thus defect-free WZ/ZB homostructures in GaP nanowires with the aim to obtain monolayer control of the ZB and WZ segment lengths. We find that the Ga concentration and the supersaturation in the catalyst particle are the key parameters determining growth kinetics. These parameters can be tuned by the gallium partial pressure and the temperature. The formation of WZ and ZB can be understood with a model based on nucleation either at the triple phase line for the WZ phase or in the center of the solid–liquid interface for the ZB phase. Furthermore, the observed delay/offset time needed to induce WZ and ZB growth after growth of the other phase can be explained within this framework.

**KEYWORDS:** semiconductor nanowire, gallium phosphide, wurtzite, zincblende, monolayer growth, supersaturation



For optical quantum information processing emission sources are needed, which can emit identical photons.<sup>1</sup> This is a challenge because quantum structures based on heterostructures always show variations in size and composition, leading to a spread in emission wavelength.<sup>2,3</sup> With nanowires, a new type of band structure engineering has become available that is based on junctions formed by different crystal structures of identical chemical composition.<sup>4–6</sup> Such advanced structures can behave as single photon sources.<sup>7</sup> The development of nanowire homostructures formed by the combination of the zincblende (ZB) and wurtzite (WZ) crystal phases has drawn a lot of attention in the past few years.<sup>4,5,8,9</sup> Gallium phosphide (GaP) in the normal cubic phase has an indirect band gap,<sup>10,11</sup> but a direct band gap in the WZ crystal structure has been theoretically predicted<sup>12–14</sup> and recently shown in WZ GaP wires by photoluminescence and electrochemical measurements.<sup>15,16</sup> Precise crystal phase control would allow the growth of crystal phase quantum well (CPQW) or quantum dot (CPQD) structures in this material system.<sup>7,12</sup> WZ/ZB homostructures and superlattices have been recently shown in different materials systems,<sup>4,8,9</sup> and photoluminescence experiments indicate size quantization effects.<sup>5</sup> However, independent control of the WZ and ZB segment lengths, crucial for design and fabrication of such advanced

quantum structures and for understanding the growth kinetics during crystal phase switching, have not been reported yet.

We note that in the WZ/ZB GaP system, electrons and holes can be confined in the WZ segment because of the predicted type I band alignment between WZ and ZB.<sup>12</sup> Large spontaneous polarization fields are, however, predicted for WZ GaP,<sup>17</sup> which can induce substantial surface charges across a thin ZB GaP segment embedded in WZ material in analogy to what has been reported for GaN.<sup>18</sup> In this case, the ZB segment will separate the electrons and holes and the thickness of this ZB segment determines the energy scales.<sup>19</sup> Sharp emission lines are observed in GaP nanowires with CPQWs, with energies defined by the addition of single ZB monolayers. A detailed study on the emission from these wires will be published separately. Controlled growth of multiple identical quantum wells at defined positions within the same nanowire may provide a route to study entangled photons in a solid state quantum system.<sup>1</sup> Therefore, it is essential to control the thickness of the ZB segment at the monolayer level. In this work, we first investigate the growth of ZB segments in WZ

Received: August 29, 2015

Revised: October 22, 2015

wires and then focus on controlling the WZ length, achieving high level of control for both crystal structures. We further show that crystal-phase formation and crystal-phase switching can be qualitatively explained by a nucleation model in which it is assumed that nucleation at the triple phase line competes with nucleation in the center of the catalyst/nanowire interface.

Arrays of 100 nm diameter and 500 nm pitch WZ GaP nanowires are grown with the VLS-growth method in a metalorganic vapor phase epitaxy (MOVPE) reactor using gold islands as a catalyst,<sup>15,20</sup> which are defined by nanoimprint lithography.<sup>21</sup> The SEM image of a typical sample in Figure 1a shows the position-controlled growth of arrays of untapered GaP wires. A schematic drawing of the WZ/ZB nanowire homostructures is shown in Figure 1b. The following protocol was developed for the growth of these structures. First, a 2.6

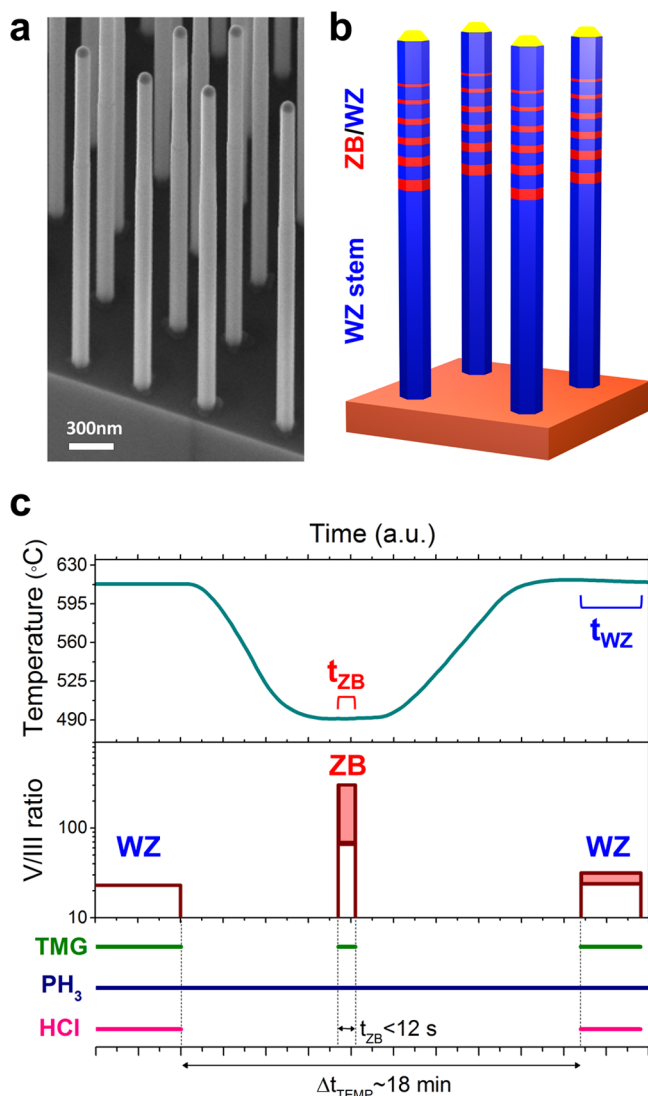


**Figure 1.** SEM image of the GaP nanowire arrays grown in the nanoimprint pattern (tilting angle 30°). (b) Schematics of the stacking of the crystal phases in the nanowires. After growth of the WZ stem several ZB segments are grown along the nanowire, alternating with WZ segments. (c) In situ temperature profile, V/III ratio, and sketch of the supply of the precursor gases during growth. The dark red shaded area indicates the range of the V/III ratios used during growth. The time interval  $t_{ZB}$  has been enlarged for better comparison with  $t_{WZ}$ .

$\mu\text{m}$  WZ GaP stem is grown at 615 °C under low V/III ratio (23), using molar fractions for the precursors of  $\chi_{\text{TMG}} = 7.42 \times 10^{-5}$ ,  $\chi_{\text{PH}_3} = 1.71 \times 10^{-3}$ , and  $\chi_{\text{HCl}} = 1.22 \times 10^{-4}$ .<sup>15</sup> A controllable crystal-phase switch is induced by tuning the growth parameters as shown in Figure 1c (see Supporting Information S1 for more details). In order to have a clean switch to the ZB phase, the gallium flow is stopped, and the growth temperature is reduced to 490 °C and the  $\text{PH}_3$  pressure is increased to a molar fraction of  $\chi_{\text{PH}_3} = 2.04 \times 10^{-3}$ .<sup>22–24</sup> When the temperature has stabilized, the gallium flow is opened again and the growth resumes under a V/III ratio of 67. No HCl gas is provided during ZB growth. Once the ZB segment growth is finished, the gallium flow is stopped, and the temperature is raised to 615 °C to grow WZ GaP. We note that phosphine is supplied during the entire process to prevent evaporation of the nanowires at these elevated temperatures.

The nanowire presented in Figure 2a is grown by repeating the process shown in Figure 1c and by using a fixed growth time for the WZ segments ( $t_{WZ} = 90$  s). To induce the growth of ZB, gallium is supplied ( $\chi_{\text{TMG}} = 3.04 \times 10^{-5}$ ) during a time interval ( $t_{ZB}$ ) varying from 3.1 to 0 s in steps of 0.4 s. The pure ZB segments in the WZ nanowire are visible in the high-resolution transmission electron microscopy (HRTEM) image in Figure 2b–c. Both interfaces in the WZ/ZB/WZ junction are atomically sharp and the domains themselves are free from stacking faults. The WZ segments are terminated by  $\{01\text{--}10\}$  side facets,<sup>15</sup> whereas during the growth of the ZB segments, nonvertical  $\{111\}$  side facets develop.<sup>25</sup> The lengths of the ZB segments are plotted in Figure 2d as a function of the Ga supply time for different TMG molar fractions. The dashed horizontal line indicates the minimum length of a ZB segment (ABC stacking) in a WZ wire, which equals 0.945 nm.<sup>26</sup> When only the temperature is lowered to 490 °C but the TMG flow is not switched on (corresponding to  $t_{ZB} = 0$  s) no ZB growth is observed. In fact, a delay time  $t_{\text{DEL}}$  occurs before the ZB nucleation starts. Here, the delay time is defined as the linear extrapolation of the plots in Figure 2d to minimum ZB length. The removal of a chlorine passivation layer present at the gold droplet after the growth of the WZ stem could partially contribute to the delay time  $t_{\text{DEL}}$  (see Supporting Information S2). For  $t > t_{\text{DEL}}$ , a growth rate  $R_{ZB} = 7.3 \pm 0.3$  nm/s is measured at  $\chi_{\text{TMG}} = 3.04 \times 10^{-5}$ . Furthermore, a reduction in the droplet diameter is observed after the growth of the first ZB segment ( $t_{ZB} = 3.1$  s), indicating a depletion of the Ga content in the gold droplet after the first cooldown/warm-up process. By contrast, for the following ZB segments the change in diameter is minimum.

In order to tune the emission wavelength of the quantum structures it is essential to have control of the dimensions at the atomic scale. For obtaining a good level of control, a low growth rate is beneficial. We first study the growth dynamics of the ZB segment as a function of the precursor flows. We observe that a change of the  $\text{PH}_3$  flow does not affect the growth rate, (see Supporting Information S3), but that the TMG pressure has a large effect, indicating that the ZB growth occurs in a Ga-limited regime. By lowering the Ga molar fraction to  $\chi_{\text{TMG}} = 1.35 \times 10^{-5}$ , the growth rate  $R_{ZB}$  decreases to  $2.8 \pm 0.2$  nm/s (7–9 ML/s), whereas the delay time increases to  $4.2 \pm 1.0$  s (see Figure 2d–f and Supporting Information S4). A critical transition is observed when the Ga molar fraction falls below  $1.35 \times 10^{-5}$ , where the growth rate increases sharply, whereas the delay time still follows a monotonic (increasing) trend. We speculate that at the lowest

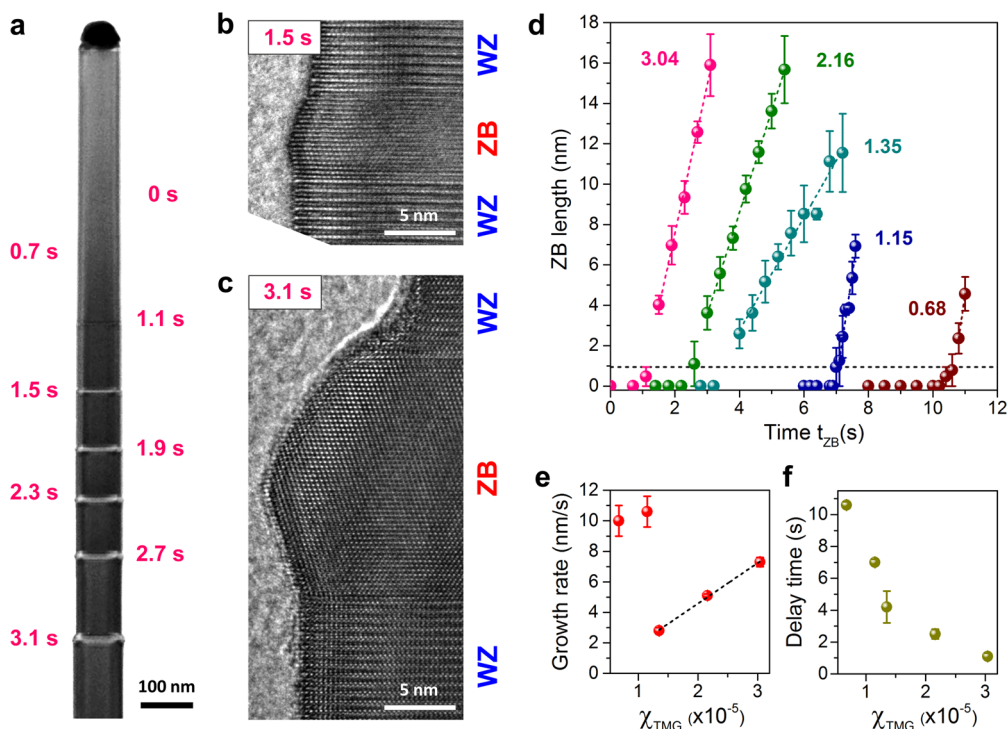


**Figure 2.** (a) TEM image of a nanowire with ZB grown for a variable time  $t_{\text{ZB}}$ , separated by WZ segments grown for fixed  $t_{\text{WZ}} = 90$  s ( $\chi_{\text{TMG}} = 3.04 \times 10^{-5}$ ). (b–c) HRTEM images of the nanowire in (a) for ZB segments grown for  $t_{\text{ZB}} = 3.1$  s (b) and  $t_{\text{ZB}} = 1.5$  s (c), showing defect-free crystal phases with atomically sharp interfaces. (d) Length of ZB segments as a function of the Ga supply time  $t_{\text{ZB}}$  for different TMG molar fractions  $\chi_{\text{TMG}}$ , indicated in units of  $1 \times 10^{-5}$ . The dashed horizontal line indicates the shortest stacking sequence for the ZB phase (ABC stacking) in a WZ wire, which is equal to 0.945 nm. (e–f) ZB growth rate  $R_{\text{ZB}}$  (e) and delay time  $t_{\text{DEL}}$  (f) as a function of the Ga molar fraction  $\chi_{\text{TMG}}$ . The error bars in (d–f) refer to a set of four nanowires measured via HRTEM.

Ga molar flows additional P is incorporated in the gold droplet, leading to an increase in the supersaturation  $\Delta\mu$  (see Supporting Information S5);<sup>27</sup> hence, a higher growth rate during the growth of the ZB segment is observed. This is undesirable because the higher growth rate reduces the control over the ZB growth. We find that up to a length of 15 nm the ZB phase is generally defect-free. For longer segments, nucleation of twin defects is observed, followed by the evolution of the growth into a mixed ZB–WZ phase, with no control of the crystal phase in this regime (see Supporting Information S6 for more details).

We explore the possibility of extending this growth mode to achieve monolayer control by using the lowest ZB growth rate of  $\sim 7$ – $9$  ML/s, which is obtained with a Ga molar fraction  $\chi_{\text{TMG}} = 1.35 \times 10^{-5}$ . In the nanowire in Figure 3a, the Ga precursor is switched on for decreasing time intervals between 4.6 and 3.4 s with steps of 0.1 s. The high-resolution scanning TEM (HRSTEM) images in Figure 3b–d show ZB segments of 3, 7, and 8 MLs, respectively. The group-V polar growth direction (B) is maintained when switching between WZ and ZB crystal structures.<sup>28</sup> In Figure 3e, the number of ZB monolayers as a function of the Ga supply time  $t_{\text{ZB}}$  for four different nanowires is shown. The following observations can be made. First, several monolayers rather than a single monolayer nucleate on average within a 0.1 s time interval, which is the resolution limit of our MOVPE machine. Recently, in situ TEM studies in a ultrahigh vacuum TEM showed that GaP nanowire growth occurs by the addition of single monolayers, providing evidence that VLS growth proceeds in a single layer-by-single layer mode.<sup>29</sup> Ideally, monolayer control might be achieved in a MOVPE reactor with switching times

shorter than 0.1 s. Second, in most of the investigated wires, the growth begins with 5–7 MLs, as shown for NW3–4. Occasionally the ZB growth starts with 3 MLs, which is the shortest possible ZB stacking segment, as seen for NW1–2. We suppose that wire-to-wire variations in diameter (compare Supporting Information S7) and in droplet supersaturation induce variations in the delay time and in the initial ZB segment length (see Figure S4 in Supporting Information), with a large effect on the number of ZB monolayers grown for a given ZB growth time. Third, close to the delay time  $t_{\text{DEL}}$  the ZB growth rate is 20–26 ML/s, which is higher than the value of 7–9 ML/s observed for longer growth times (compare Figures 2d–e and S4). Thus, even though the ZB growth rate has been reduced by lowering the Ga flow, the above results show that growth of homostructures with control at the monolayer level is still a challenge.

The formation of the WZ phase has been investigated in a similar way. The growth rate of the WZ phase is studied by growing WZ segments for different time intervals separated by 10 nm ZB markers, as shown in Figure 4a–b (see Supporting Information S8 for more details). The lengths of the WZ segments averaged over four different wires are plotted in Figure 4c as a function of the Ga supply time  $t_{\text{WZ}}$ , and the data points from one single wire are shown in the inset in Figure 4c. When a Ga molar fraction of  $\chi_{\text{TMG}} = 7.42 \times 10^{-5}$  is used, a constant WZ length of  $L_{\text{WZ}} = 7 \pm 3$  nm is observed for all supply times below the offset time  $t_{\text{OFF}} = 14 \pm 2$  s, whereas above this value, an increase in the WZ segment length is observed (blue dots in Figure 4c). Instead, when the Ga molar fraction is reduced to  $\chi_{\text{TMG}} = 5.40 \times 10^{-5}$ , the offset time  $t_{\text{OFF}}$  increases to  $\sim 100$  s (dark red dots in Figure 4c), whereas  $L_{\text{WZ}}$

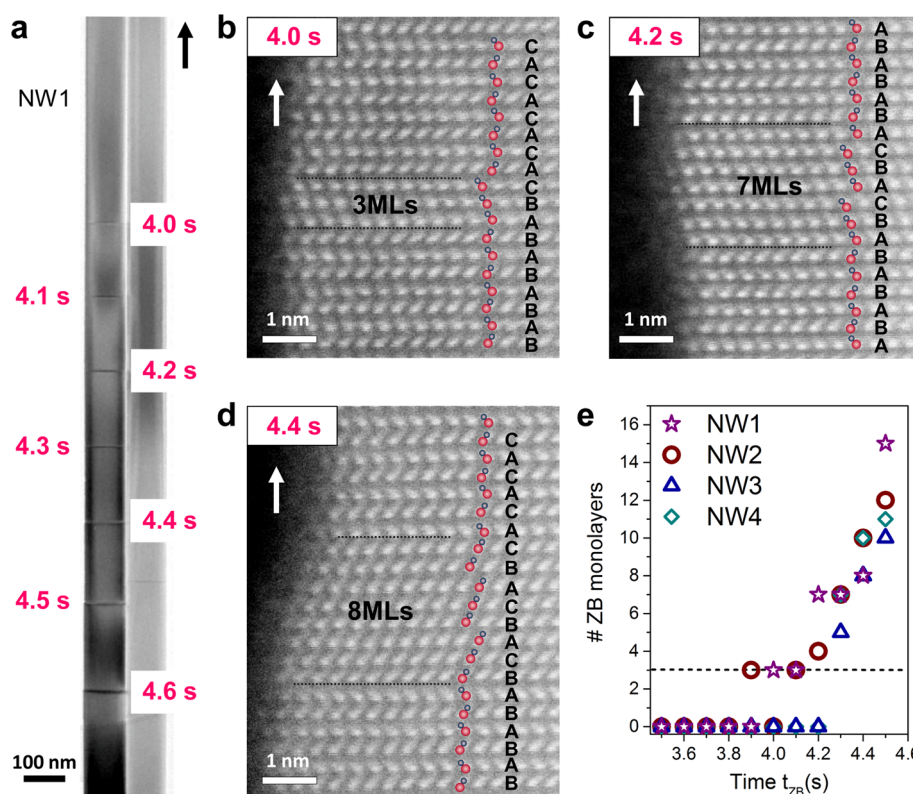


**Figure 3.** (a) TEM image of a nanowire grown using 0.1 s steps for the Ga supply time  $t_{ZB}$  and a TMG molar fraction  $\chi_{TMG} = 1.35 \times 10^{-5}$ . (b–d) HR-STEM images showing controlled ZB segment lengths of 3, 7, and 8 MLs. The red and blue dots indicate the Ga and P atoms, respectively, while arrows indicate the growth direction. (e) Number of ZB monolayers as a function of the Ga supply time  $t_{ZB}$  for four different nanowires. The dashed line corresponds to the shortest stacking sequence for the ZB phase in a WZ wire, which has a length of 3 MLs (ABC stacking). The diameters of the four nanowires are in the range 96–106 nm.

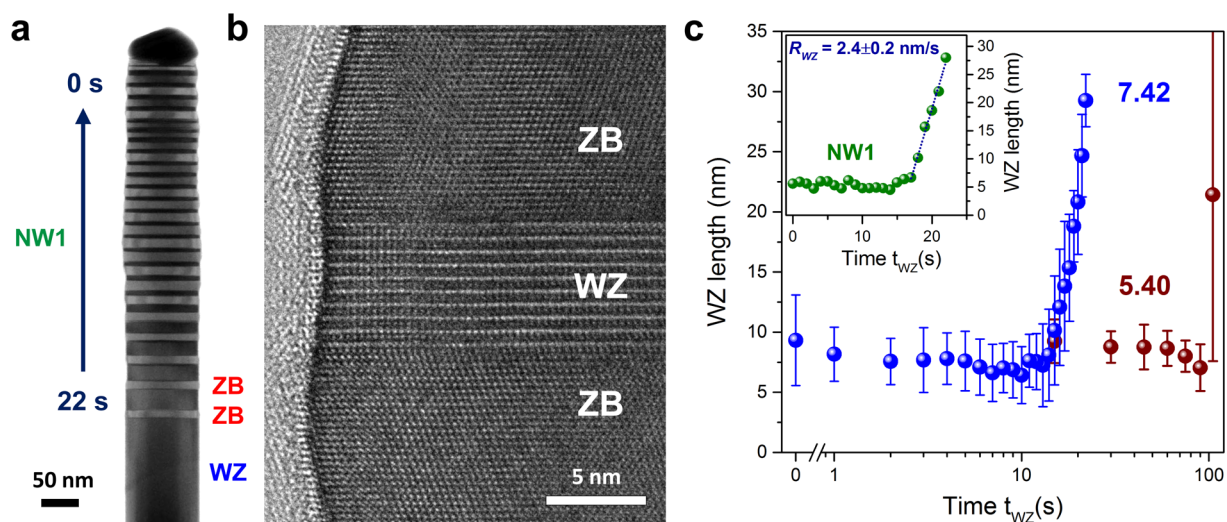


**Figure 4.** (a) TEM image of a nanowire with WZ segments grown for different Ga supply times  $t_{WZ}$  using a TMG molar fraction  $\chi_{TMG} = 7.42 \times 10^{-5}$ . The ZB segments grown for a fixed time  $t_{ZB}$  are used as markers. (b) HRTEM image showing *parasitically* grown WZ in between two ZB segments. (c) WZ length as a function of  $t_{WZ}$  for two different TMG molar fractions  $\chi_{TMG}$ , indicated in units of  $1 \times 10^{-5}$ . The error bars refer to a set of four nanowires measured via HRTEM. Inset: WZ length as a function of  $t_{WZ}$  for the nanowire in (a).

does not change as long as  $t_{WZ} < t_{OFF}$ . The fact that  $L_{WZ}$  is independent of both  $t_{WZ}$  (for  $t_{WZ} < t_{OFF}$ ) and  $\chi_{TMG}$  indicates that this constant-length WZ segment is formed by so-called *parasitic* WZ growth, that is, growth in the absence of Ga supply, either when the temperature is still at 490 °C or during its increase from 490 to 615 °C (cf. Figure 1c). Apparently, residual gallium in the gold droplet is able to induce growth of

this short segment with WZ crystal structure,<sup>8</sup> whereas further *regular* WZ growth, that is, induced by the supplied Ga, starts only after the  $\chi_{TMG}$  dependent offset time. The formation of *parasitic* WZ will be discussed in more detail below in the context of Figure 5. Variations in the wire diameter affect  $L_{WZ}$  (see Supporting Information S8); hence, the patterned substrate plays a key role in minimizing the spread in segment

lengths.<sup>30</sup> The inset in Figure 4c shows that the variation of the parasitic WZ lengths within a single nanowire is minimal, substantially smaller than that between different nanowires. This demonstrates the high reproducibility attained by the growth protocol in itself.

In order to understand the crystal switch dynamics, including the delay and offset times, and the parasitic WZ growth, we will use below a kinetic nucleation model proposed by Breuer et al.<sup>31</sup> An important parameter in the growth kinetics is the gallium concentration in the Au–Ga droplet,  $c_{\text{Ga}}$ , from which we can estimate the supersaturation,  $\Delta\mu$ , of the liquid with respect to the solid phase during growth.<sup>32</sup> To determine this concentration, the sample is cooled down to room temperature under arsine ( $\text{AsH}_3$ ) instead of  $\text{PH}_3$ ,<sup>33</sup> such that a GaAs segment is formed. From TEM imaging and energy-dispersive X-ray (EDX) analysis, the volume of the GaAs segment and the residual Ga concentration in the droplet are determined, respectively, which allows estimating the total Ga concentration  $c_{\text{Ga}}$  in the droplet during growth. Three instants in the nanowire growth cycle have been studied by this method: during growth of the WZ stem, during ZB growth, and during regular WZ growth subsequent to the growth of a ZB segment (see Supporting Information S9 for more details). The measured values for  $c_{\text{Ga}}$  are listed in Table 1. The Ga concentration during

**Table 1. Values for the Ga Content and Supersaturation  $\Delta\mu$  at the Gold Droplet for the WZ, ZB,  $\psi$ , and WZ' Phases, Calculated According to Ref 27 for the Measured Ga Concentrations, with  $c_{\text{p}} = 0.01$ <sup>a</sup>**

	Phase	T (°C)	$c_{\text{Ga}}$ (%)	$\Delta\mu$ (meV)	$\Delta\mu \cdot k_{\text{B}}T$ ( $10^3 \cdot \text{meV}^2$ )
1 2 3	WZ	615	37±2	320±15	24.5±0.4
	ZB	490	27±2	350±15	23.0±0.5
	$\psi$	615	22±2	120±25	9.6±0.3
	WZ'	615	37±2	320±15	24.5±0.4

<sup>a</sup>Curved arrows and numbers indicate the transitions between the different phases.

ZB growth is lower ( $\sim 27\%$ ) than that during WZ growth ( $\sim 37\%$ ), whereas after parasitic WZ growth (labeled as  $\psi$ ), the Ga content is the lowest ( $\sim 22\%$ , see Supporting Information S10).

The supersaturation  $\Delta\mu$  as a function of the Ga concentration is now calculated for the two growth temperatures by using the thermodynamical model developed by Glas,<sup>27</sup> under the assumption that the P concentration remains constant and is equal to 1%, and the result is shown in Figure 5a and Table 1 (see Supporting Information S5 for more details). Importantly, a decrease in temperature results in an increase of the supersaturation  $\Delta\mu$ . With the aid of this plot and the measured Ga concentrations the transitions, labeled 1, 2, and 3 in Table 1, between the stages of WZ growth and ZB growth can be described in more detail. Transition 1 is the transition from stationary regular (i.e., with the TMG flow on) WZ growth (either of the stem or of a segment in a later growth cycle) to stationary ZB growth, during which the sample is cooled from 615 to 490 °C in the absence of TMG flow (cf. Figure 1c). We note that evaporation of Ga from the gold droplet is predominant at 615 °C (see Supporting Information S11). Thus, when TMG is switched off, fast depletion of Ga (on a time scale of  $\sim 6$  s) from the droplet

occurs toward a Ga concentration of  $\sim 22\%$  (transition 1a), quenching growth already well before that value has been reached. The subsequent temperature lowering to 490 °C leads to an increase in  $\Delta\mu$  (transition 1b). Next, the TMG flow is switched on at 490 °C, and during the delay time  $t_{\text{DEL}}$ , the droplet is rapidly refilled in Ga content (see Supporting Information S12), eventually reaching the value of  $\sim 27\%$  during (regular) ZB growth (transition 1c). Transition 2 is the transition from ZB growth to the state  $\psi$  of high T and low  $\Delta\mu$ . Because there is almost no Ga evaporation at 490 °C (see Supporting Information S11), initially both the Ga concentration and  $\Delta\mu$  can decrease only a little due to parasitic growth after TMG has been switched off. Only during the heat-up stage from 490 to 615 °C, with the TMG flow still off, the temperature increase makes  $\Delta\mu$  decrease significantly, whereas the enhanced evaporation of Ga at higher temperature lowers the Ga content to  $\sim 22\%$ . We argue below, when discussing Figure 5d, that in the initial stage of transition 2 residual Ga in the droplet<sup>8</sup> induces parasitic WZ growth. Transition 3 is the evolution from the state  $\psi$  to regular WZ growth. In order to restart the WZ growth TMG is supplied at 615 °C, and  $c_{\text{Ga}}$  returns to the stationary value for WZ growth of  $\sim 37\%$ . As Table 1 and Figure 5 show, ZB growth takes place at supersaturation values of 335–365 meV (or even higher if the reduced P desorption at 490 °C leads to an enhanced P concentration), whereas regular WZ growth occurs for  $\Delta\mu$  in the range 305–335 meV. Thus, the ZB phase forms at higher supersaturation than the WZ phase. This observation is in clear contradiction to the behavior expected for nucleation at the triple-phase line (TPL) from the well-known model developed by Glas et al.,<sup>32</sup> which predicts ZB formation to occur at lower  $\Delta\mu$  than WZ formation.<sup>24,29,31</sup>

To resolve this contradiction, we propose that only WZ nucleation occurs at the TPL, whereas the nucleation of ZB takes place in the center (C) of the droplet-wire (liquid–solid) interface. Center nucleation was recently put forward to explain ZB growth of GaAs nanowires at high Ga concentration.<sup>34</sup> However, the underlying model developed by Dubrovskii<sup>35,36</sup> apparently entails a strong dependence of the growth rate on the group V flow as well as larger Ga concentration for ZB growth than for WZ growth, both in contradiction with our present findings. Therefore, we base our proposal upon the extension of the model by Glas et al.<sup>32</sup> that takes the larger number of nucleation sites available for C-nucleation than for TPL-nucleation into account.<sup>31</sup> It starts from the familiar assumption that growth takes place in a layer-by-layer fashion, with the nucleation rate  $R_{\text{X}}$  given by  $R_{\text{X}} = b N_{\text{X}}(D) \exp\{-\Delta G_{\text{X}}^*/k_{\text{B}}T\}$ , where  $\Delta G_{\text{X}}^* = A_{\text{X}}/\Delta\mu$  is the free energy for nucleation of phase X, with  $A_{\text{X}}$  characterizing the surface energy of the nucleus sidewall,  $N_{\text{X}}(D)$  the number of sites available for nucleation, and  $b$  a kinetic constant. Because  $N_{\text{X}}(D)$  scales with the diameter  $D$  of the nanowire as  $D^2$  for C-nucleation and as  $D$  for TPL-nucleation, the difference between the free nucleation energies (generally  $\Delta G_{\text{WZ,TPL}}^* < \Delta G_{\text{ZB,C}}^*$ ) can be overcome, for sufficiently thick wires, by the difference between the number of potential nucleation sites. This defines a phase boundary  $\Delta\mu_{\text{C}}(T)$  in the temperature–supersaturation plane, given approximately by  $T = [(A_{\text{ZB,C}} - A_{\text{WZ,TPL}})/(k_{\text{B}} \cdot \ln(D/2a_0))]/\Delta\mu$ , with  $a_0$  the lattice constant in the GaP (111) interface plane. Because the surface energies  $A_{\text{X}}$  of the sidewalls are temperature dependent, the boundary is in fact substantially steeper than suggested by the  $1/\Delta\mu$  dependence. A typical phase diagram calculated according to this model is shown in

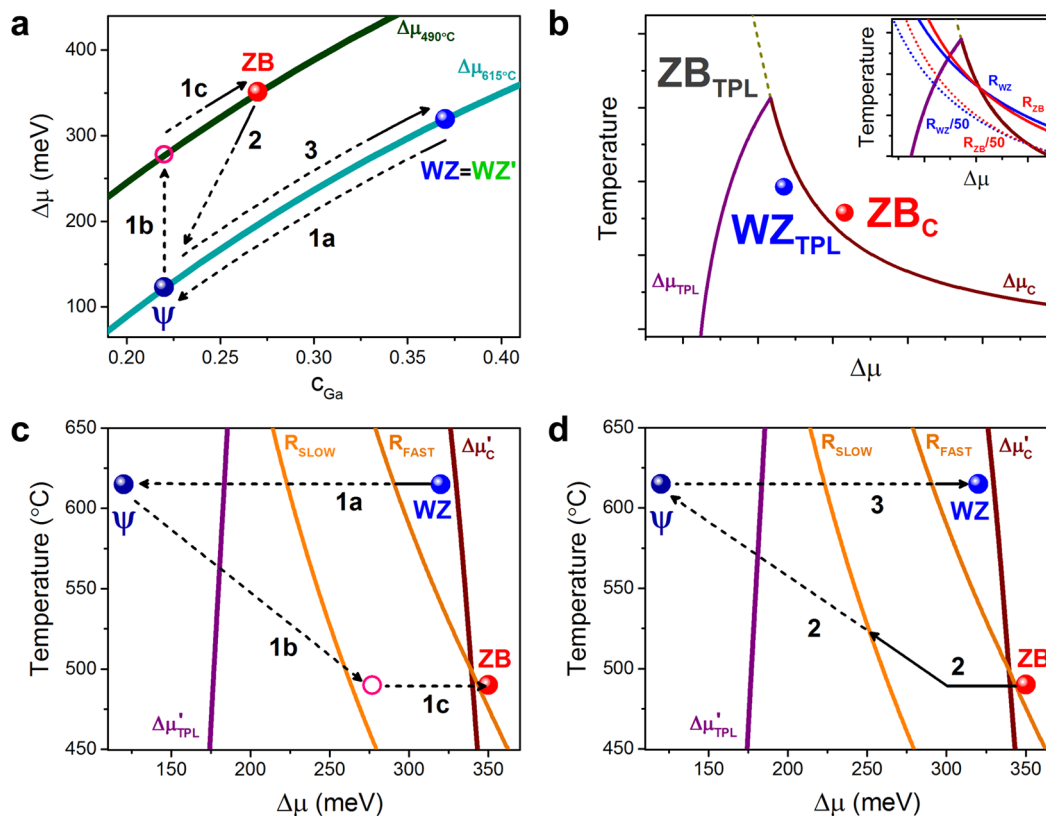


**Figure 5.** (a) Plot of  $\Delta\mu$  as a function of Ga content calculated according to ref 27, for temperatures of 490 and 615 °C, and  $c_p = 0.01$ . This assumption of constant high P vapor pressure<sup>38</sup> may have led to an overestimation of  $\Delta\mu$  at 615 °C, correction of which would give a bigger difference in  $\Delta\mu$  between WZ and ZB growth. (b) Phase diagram for nanowire growth according to the nucleation model including the effect from the number of nucleation sites.<sup>31</sup> The inset shows in addition lines of equal growth rate ( $R$ ) for [WZ,TPL] (blue curves) and [ZB,C] (red curves) at two growth rates differing by a factor 50. Parameters are chosen such as to enhance qualitative features. (c–d) Phase diagrams for GaP nanowire growth during the WZ–ZB (c) and ZB–WZ (d) transitions. The arrows represent the experimental trajectory, shown in (a). Solid arrows represent changes in ( $T$ ;  $c_{Ga}$ ;  $\Delta\mu$ ) accompanied by growth, whereas dashed arrows represent such changes in the absence of growth. Model parameters for surface energy densities: solid–liquid,  $\gamma_{SL} = 0.60 \text{ J/m}^2$ , solid–vapor,  $\gamma_{SV}^{ZB} = 0.75 \text{ J/m}^2$ ,  $\gamma_{SV}^{WZ} = 0.67 \text{ J/m}^2$ ; liquid–vapor,  $\gamma_{LV} = c_{Ga}^{Ga} \gamma_{LV}^{Ga} + c_{Au}^{Au} \gamma_{LV}^{Au}$ ;  $\gamma_{LV}^{Ga} = \gamma_{LV,m}^{Ga} - c_{LV,m}^{Ga} (T - T_m^{Ga})$  where  $\gamma_{LV,m}^{Ga} = 0.711 \text{ J/m}^2$ ,  $c_{LV,m}^{Ga} = 7 \cdot 10^{-5}$ ,  $T_m^{Ga} = 30 \text{ °C}$ ,  $\gamma_{LV,m}^{Au} = 1.145 \text{ J/m}^2$ ,  $c_{LV,m}^{Au} = 20 \cdot 10^{-5}$ ,  $T_m^{Au} = 1065 \text{ °C}$ ; hydrogen binding energy = 2.9 eV; nanowire diameter  $D = 100 \text{ nm}$ ; the  $\Delta\mu$  values from the model are rescaled by a factor 0.56.

Figure 5b (see Supporting Information S13 for more details). There are three different regions in the phase diagram: (i) ZB nucleation at the TPL ( $\Delta\mu < \Delta\mu_{TPL}$ ); (ii) WZ nucleation at the TPL ( $\Delta\mu_{TPL} < \Delta\mu < \Delta\mu_C$ ); (iii) ZB nucleation at the center of the droplet ( $\Delta\mu > \Delta\mu_C$ ). So,  $\Delta\mu_{TPL}$  is the boundary predicted by Glas et al.,<sup>32</sup> whereas  $\Delta\mu_C$  is the boundary discussed above. Figure 5b reveals the idea underlying our proposal: when the temperature is lowered from 615 to 490 °C, the resulting increase in supersaturation  $\Delta\mu$  at the gold droplet,<sup>27</sup> which is possibly enhanced by an increase in P content produced by the reduced P desorption<sup>34,37,38</sup> (see Supporting Information S5), may lead to *crossing the critical boundary*  $\Delta\mu_C$ . This leads to switching from stationary TPL-nucleation of WZ to stationary C-nucleation of ZB, as illustrated by the locations of the blue and red points. In addition, in the inset in Figure 5b lines with a constant growth rate (*equi-growth-rate lines*) for ZB and WZ are shown. Note that the growth rate decreases rapidly by moving downward and leftward in Figure 5b, that is, when the product  $\Delta\mu \cdot k_B T$  gets smaller, eventually reaching extremely low values where the growth stops. Thus, to the left of a suitably chosen *zero-growth-rate line* no growth takes place.

The three transitions between WZ and ZB growth can now be understood in detail, based on this model with the help of Figure 5c–d. In those figures, the supersaturation–Ga

concentration trajectory of Figure 5a is transformed into a temperature–supersaturation trajectory and then superimposed upon the relevant part of a phase diagram like shown in Figure 5b, now calculated for parameters plausible for GaP and then rescaled with respect to  $\Delta\mu$ , as discussed below. Because, quite generally, growth does not start as long as  $\Delta\mu$  increases faster due to Ga supply than it would decrease due to Ga consumption owing to growth (and similarly only stops as soon as  $\Delta\mu$  decreases faster due to Ga evaporation than it decreases due to Ga consumption owing to growth), two different *zero-growth-rate lines* must be considered. The line  $R_{FAST}$  ( $R_{SLOW}$ ) where the growth rate is only moderately lower (lower by a factor 50) than during stationary growth, relates to refilling/depletion in the order of seconds (in the order of minutes). At transition 1a, when the TMG flow has been switched off after *regular* WZ growth, the evaporation of Ga, predominant at this high temperature (see Supporting Information S5), rapidly reduces  $c_{Ga}$ . This results in  $\Delta\mu$  reaching the line  $R_{FAST}$  in less than a second, thus suppressing *parasitic* WZ growth, which otherwise might occur here because  $\Delta\mu_{TPL} < \Delta\mu < \Delta\mu_C$ . Note that it is irrelevant that  $\Delta\mu$  eventually drops below  $\Delta\mu_{TPL}$  when approaching  $\psi$  as there is no growth in this regime. Next, the sample is cooled down to 490 °C, so  $T$  decreases and  $\Delta\mu$  increases again, but there is no growth

(transition 1b). After the TMG flow has been switched on at 490 °C, the droplet is refilled by Ga within a few seconds during the delay time  $t_{\text{DEL}}$  (see Supporting Information S12), with  $\Delta\mu$  crossing  $\Delta\mu_{\text{C}}$  shortly before reaching  $R_{\text{FAST}}$ , so that growth starts only when  $\Delta\mu$  is already well above  $\Delta\mu_{\text{C}}$ , thus yielding pure ZB material and a sharp WZ/ZB interface (transition 1c). The observation of mixed phase material for longer growth times (see Supporting Information Figure S3) indicates a (slow) reduction of supersaturation during ZB growth, resulting in  $\Delta\mu \sim \Delta\mu_{\text{C}}$  (without growth having been interrupted at  $R_{\text{FAST}}$ ), hence in similar nucleation probabilities for ZB and WZ nuclei. This reduction can be attributed to a progressive change in side facets, contact angle, and a possible depletion of Ga (see Figure 2b), which then affect the surface energies of the gold droplet, hence  $\Delta\mu$ . At transition 2 in Figure 5d, when TMG has been switched off, Ga depletion of the droplet is entirely due to growth and thus keeps pace with it, because there is almost no Ga evaporation (Supporting Information S11). Hence, growth continues to the left of  $R_{\text{FAST}}$  and next turns into *parasitic* WZ growth when  $\Delta\mu < \Delta\mu_{\text{C}}$ , at an ever lower growth rate. During heat up from 490 to 615 °C, the *parasitic* WZ growth continues until  $R_{\text{SLOW}}$  is reached. The increased evaporation of Ga with rising temperature further reduces the Ga content in the droplet to  $\sim 22\%$ , reaching  $\psi$ . At transition 3, when the TMG flow is switched on at 615 °C in order to restart *regular* WZ growth, an offset time  $t_{\text{OFF}}$  of the order of 10 s is required to refill the droplet and make  $\Delta\mu$  reach  $R_{\text{FAST}}$ , where growth starts evolving soon into stationary WZ growth.

The discrepancy between the values for  $\Delta\mu_{\text{TPL}}$  and  $\Delta\mu_{\text{C}}$  predicted by the nucleation model for plausible GaP parameters (see Supporting Information Table T3) and the *experimental* values, that is, as calculated according to ref 27 from the measured Ga concentrations in the droplet, requires rescaling of the calculated  $\Delta\mu$  axis in Figure 5c–d. However, the values from the nucleation model are strongly dependent on the material parameters such as the surface energies, which are not known accurately, whereas the experimental values are highly sensitive to the even less well-known P concentration in the droplet.<sup>27</sup> The nucleation model<sup>31</sup> as applied here qualitatively describes and explains the crystal phase switching between ZB and WZ structure in VLS nanowire growth. One additional observation lends further support to this interpretation: the observed increase in purity of the WZ phase for increasing growth temperature<sup>39</sup> is explained by the resulting reduction of the supersaturation  $\Delta\mu$  ever further below  $\Delta\mu_{\text{C}}$  (see Figure 5b), which indeed ought to lead to defect-free WZ growth.

The crystal-phase switching method developed in this paper for arrays of nanowires allows the growth of atomically sharp interfaces between alternating single crystalline ZB and WZ segments along the nanowire length, with position of the junction and length of the segments controlled by the supply of the Ga precursor and growth temperature. This growth method does not affect the nanowire diameter and does not induce any tapering. The patterned substrate is a key factor in order to achieve highly reproducible crystal-phase switching, minimizing fluctuations in diameter and local V/III ratio of the nanowires. Upon combining a kinetic nucleation model that takes the number of available nucleation sites into account with a set of measured Ga concentrations in the gold droplet during the various stages of growth, we propose that WZ nucleation takes place at the triple-phase line (TPL) and that ZB nucleation occurs at the center (C) of the droplet–wire (liquid–solid)

interface. We suggest that this holds not just for GaP, investigated here, but for all III–V compounds where such crystal-phase switching occurs in VLS growth.

## ■ ASSOCIATED CONTENT

### Supporting Information

The Supporting Information is available free of charge on the ACS Publications website at DOI: 10.1021/acs.nanolett.5b03484.

Additional information on growth conditions, sample characterization, and nucleation model are provided. (PDF)

## ■ AUTHOR INFORMATION

### Corresponding Author

\*E-mail: s.assali@tue.nl.

### Notes

The authors declare no competing financial interest.

## ■ ACKNOWLEDGMENTS

The authors thank P. J. van Veldhoven for the technical support with the MOVPE reactor, A. Li, S. Conesa-Boj, and S. Breuer for the fruitful discussion. This work was supported by the Dutch Organization for Scientific Research (NWO-VICI 700.10.441), and by the Dutch Technology Foundation (STW 12744) and Philips Research. Solliance is acknowledged for funding the TEM facility. D.S.O. acknowledges FAPESP (2013/24902-3) for funding his scholarship.

## ■ REFERENCES

- (1) Versteegh, M. A. M.; Reimer, M. E.; Jöns, K. D.; Dalacu, D.; Poole, P. J.; Gulinatti, A.; Giudice, A.; Zwiller, V. *Nat. Commun.* **2014**, *5*, 5298.
- (2) Reimer, M. E.; Bulgarini, G.; Akopian, N.; Hocevar, M.; Bavinck, M. B.; Verheijen, M. A.; Bakkers, E. P. A. M.; Kouwenhoven, L. P.; Zwiller, V. *Nat. Commun.* **2012**, *3*, 737.
- (3) Juska, G.; Dimastrodonato, V.; Mereni, L. O.; Gocalinska, A.; Pelucchi, E. *Nat. Photonics* **2013**, *7*, 527–531.
- (4) Dick, K. A.; Thelander, C.; Samuelson, L.; Caroff, P. *Nano Lett.* **2010**, *10*, 3494–3499.
- (5) Vainorius, N.; Lehmann, S.; Jacobsson, D.; Samuelson, L.; Dick, K. A.; Pistol, M.-E. *Nano Lett.* **2015**, *15*, 2652–2656.
- (6) Fiorentini, V.; Bernardini, F.; Della Sala, F.; Di Carlo, A.; Lugli, P. *Phys. Rev. B: Condens. Matter Mater. Phys.* **1999**, *60*, 8849–8858.
- (7) Akopian, N.; Patriarche, G.; Liu, L.; Zwiller, V.; Harmand, J.-C. *Nano Lett.* **2010**, *10*, 1198–1201.
- (8) Bolinsson, J.; Caroff, P.; Mandl, B.; Dick, K. A. *Nanotechnology* **2011**, *22*, 265606.
- (9) Lehmann, S.; Jacobsson, D.; Dick, K. A. *Nanotechnology* **2015**, *26*, 301001.
- (10) Dean, P.; Thomas, D. *Phys. Rev.* **1966**, *150*, 690–703.
- (11) Morgan, T. N. *Phys. Rev. Lett.* **1968**, *21*, 819–823.
- (12) Belabbes, A.; Panse, C.; Furthmüller, J.; Bechstedt, F. *Phys. Rev. B: Condens. Matter Mater. Phys.* **2012**, *86*, 075208–1–12.
- (13) Bechstedt, F.; Belabbes, A. *J. Phys.: Condens. Matter* **2013**, *25*, 273201.
- (14) De, A.; Pryor, C. E. *Phys. Rev. B: Condens. Matter Mater. Phys.* **2010**, *81*, 155210.
- (15) Assali, S.; Zardo, I.; Plissard, S.; Kriegner, D.; Verheijen, M. A.; Bauer, G.; Meijerink, A.; Belabbes, A.; Bechstedt, F.; Haverkort, J. E. M.; Bakkers, E. P. A. M. *Nano Lett.* **2013**, *13*, 1559–1563.
- (16) Standing, A.; Assali, S.; Gao, L.; Verheijen, M. A.; van Dam, D.; Cui, Y.; Notten, P. H. L.; Haverkort, J. E. M.; Bakkers, E. P. A. M. *Nat. Commun.* **2015**, *6*, 7824.

- (17) Belabbes, A.; Furthmüller, J.; Bechstedt, F. *Phys. Rev. B: Condens. Matter Mater. Phys.* **2013**, *87*, 035305.
- (18) Lähnemann, J.; Brandt, O.; Jahn, U.; Pfüller, C.; Roder, C.; Dogan, P.; Grosse, F.; Belabbes, A.; Bechstedt, F.; Trampert, A.; Geelhaar, L. *Phys. Rev. B: Condens. Matter Mater. Phys.* **2012**, *86*, 081302(R)– 1–5.
- (19) Lähnemann, J.; Jahn, U.; Brandt, O.; Flissikowski, T.; Dogan, P.; Grahn, H. T. *J. Phys. D: Appl. Phys.* **2014**, *47*, 423001.
- (20) Wagner, R. S.; Ellis, W. C. *Appl. Phys. Lett.* **1964**, *4*, 89–90.
- (21) Martensson, T.; Carlberg, P.; Borgström, M.; Montelius, L.; Seifert, W.; Samuelson, L. *Nano Lett.* **2004**, *4*, 699–702.
- (22) Verheijen, M. A.; Algra, R. E.; Borgström, M. T.; Immink, G.; Sourty, E.; van Enckevort, W. J. P.; Vlieg, E.; Bakkers, E. P. A. M. *Nano Lett.* **2007**, *7*, 3051–3055.
- (23) Algra, R. E.; Verheijen, M. A.; Feiner, L.-F.; Immink, G. G. W.; van Enckevort, W. J. P.; Vlieg, E.; Bakkers, E. P. A. M. *Nano Lett.* **2011**, *11*, 1259–1264.
- (24) Joyce, H. J.; Wong-Leung, J.; Gao, Q.; Tan, H. H.; Jagadish, C. *Nano Lett.* **2010**, *10*, 908–915.
- (25) Algra, R. E.; Verheijen, M. A.; Feiner, L. F.; Immink, G. G. W.; Theissmann, R.; Van Enckevort, W. J. P.; Vlieg, E.; Bakkers, E. P. A. M. *Nano Lett.* **2010**, *10*, 2349–2356.
- (26) Caroff, P.; Dick, K. A.; Johansson, J.; Messing, M. E.; Deppert, K.; Samuelson, L. *Nat. Nanotechnol.* **2009**, *4*, 50–55.
- (27) Glas, F. J. *Appl. Phys.* **2010**, *108*, 073506.
- (28) de la Mata, M.; Magen, C.; Gazquez, J.; Utama, M. I. B.; Heiss, M.; Lopatin, S.; Furtmayr, F.; Fernandez-Rojas, C. J.; Peng, B.; Morante, J. R.; Rurali, R.; Eickhoff, M.; Fontcuberta i Morral, A.; Xiong, Q.; Arbiol, J. *Nano Lett.* **2012**, *12*, 2579–2586.
- (29) Chou, Y.-C.; Hillerich, K.; Tersoff, J.; Reuter, M. C.; Dick, K. A.; Ross, F. M. *Science (Washington, DC, U. S.)* **2014**, *343*, 281–284.
- (30) Borgström, M. T.; Immink, G.; Ketelaars, B.; Algra, R.; Bakkers, E. P. A. M. *Nat. Nanotechnol.* **2007**, *2*, 541–544.
- (31) Breuer, S.; Feiner, L.-F.; Trampert, A.; Geelhaar, L. In *Book of Abstracts 6th Nanowire Growth Workshop*, 4–6 June 2012, St. Petersburg, Russia **2012**, *44*.
- (32) Glas, F.; Harmand, J.-C.; Patriarche, G. *Phys. Rev. Lett.* **2007**, *99*, 146101.
- (33) Wang, J.; Plissard, S. R.; Verheijen, M. A.; Feiner, L.-F.; Cavalli, A.; Bakkers, E. P. A. M. *Nano Lett.* **2013**, *13*, 3802–3806.
- (34) Gil, E.; Dubrovskii, V. G.; Avit, G.; André, Y.; Leroux, C.; Lekhal, K.; Grecenkov, J.; Trassoudaine, A.; Castelluci, D.; Monier, G.; Ramdani, R. M.; Robert-Goumet, C.; Bideux, L.; Harmand, J. C.; Glas, F. *Nano Lett.* **2014**, *14*, 3938–3944.
- (35) Dubrovskii, V. G.; Grecenkov, J. *Cryst. Growth Des.* **2015**, *15*, 340–347.
- (36) Dubrovskii, V. G. *J. Chem. Phys.* **2015**, *142*, 204702.
- (37) Glas, F.; Ramdani, M. R.; Patriarche, G.; Harmand, J. C. *Phys. Rev. B: Condens. Matter Mater. Phys.* **2013**, *88*, 1–14.
- (38) Okamoto, H.; Massalski, T. B. *Bull. Alloy Phase Diagrams* **1984**, *5*, 490–491.
- (39) Assali, S.; Zardo, I.; Haverkort, J. E. M.; Bakkers, E. P. A. M. Direct band gap wurtzite semiconductor nanowires. U.S. Patent 20140230720, 2014.